UC Berkeley

UC Berkeley Previously Published Works

Title

Simultaneous Positron Emission Tomography and Molecular Magnetic Resonance Imaging of Cardiopulmonary Fibrosis in a Mouse Model of Left Ventricular Dysfunction.

Permalink

https://escholarship.org/uc/item/3r92g0mh

Journal

Journal of the American Heart Association: Cardiovascular and Cerebrovascular Disease, 13(14)

Authors

Moon, Brianna

Zhou, Iris

Ning, Yingying

et al.

Publication Date

2024-07-16

DOI

10.1161/JAHA.124.034363

Peer reviewed

eScholarship.org Powered by the California Digital Library
University of California

Journal of the American Heart Association

ORIGINAL RESEARCH

Simultaneous Positron Emission Tomography and Molecular Magnetic Resonance Imaging of Cardiopulmonary Fibrosis in a Mouse Model of Left Ventricular Dysfunction

Brianna F. Moon, PhD; Iris Y. Zhou, PhD; Yingying Ning, PhD; Yin-Ching I. Chen, PhD; Mariane Le Fur, PhD; Sergey Shuvaev, PhD; Eman A. Akam, PhD; Hua Ma, PhD; Cesar Molinos Solsona, MEng, MSc; Jonah Weigand-Whittier, BS; Nicholas Rotile, BA; Lida P. Hariri, MD, PhD; Matthew Drummond, BSN, RN; Avery T. Boice, BS; Samantha E. Zygmont, BS; Yamini Sharma, PhD; Rod R. Warburton, BS; Gregory L. Martin, BS; Robert M. Blanton, MD, MA; Barry L. Fanburg, MD; Nicholas S. Hill, MD; Peter Caravan, PhD; Krishna C. Penumatsa, PhD

BACKGROUND: Aging-associated left ventricular dysfunction promotes cardiopulmonary fibrogenic remodeling, Group 2 pulmonary hypertension (PH), and right ventricular failure. At the time of diagnosis, cardiac function has declined, and cardiopulmonary fibrosis has often developed. Here, we sought to develop a molecular positron emission tomography (PET)–magnetic resonance imaging (MRI) protocol to detect both cardiopulmonary fibrosis and fibrotic disease activity in a left ventricular dysfunction model.

METHODS AND RESULTS: Left ventricular dysfunction was induced by transverse aortic constriction (TAC) in 6-month-old senescence-accelerated prone mice, a subset of mice that received sham surgery. Three weeks after surgery, mice underwent simultaneous PET-MRI at 4.7 T. Collagen-targeted PET and fibrogenesis magnetic resonance (MR) probes were intravenously administered. PET signal was computed as myocardium- or lung-to-muscle ratio. Percent signal intensity increase and Δ lung-to-muscle ratio were computed from the pre-/postinjection magnetic resonance images. Elevated allysine in the heart (P=0.02) and lungs (P=0.17) of TAC mice corresponded to an increase in myocardial magnetic resonance imaging percent signal intensity increase (P<0.0001) and Δlung-to-muscle ratio (P<0.0001). Hydroxyproline in the heart (P<0.0001) and lungs (P<0.01) were elevated in TAC mice, which corresponded to an increase in heart (myocardium-to-muscle ratio, P=0.02) and lung (lung-to-muscle ratio, P<0.001) PET measurements. Pressure-volume loop and echocardiography demonstrated adverse left ventricular remodeling, function, and increased right ventricular systolic pressure in TAC mice.

CONCLUSIONS: Administration of collagen-targeted PET and allysine-targeted MR probes led to elevated PET–magnetic resonance imaging signals in the myocardium and lungs of TAC mice. The study demonstrates the potential to detect fibrosis and fibrogenesis in cardiopulmonary disease through a dual molecular PET–magnetic resonance imaging protocol.

Key Words: [68Ga]CBP8 ■ allysine ■ collagen ■ fibrogenesis ■ heart failure ■ pulmonary hypertension

Correspondence to: Peter Caravan, PhD, A.A. Martinos Center for Biomedical Imaging, Massachusetts General Hospital, Harvard Medical School, Suite 2301, 149 Thirteenth St, Charlestown, MA 02129. Email: pcaravan@mgh.harvard.edu and Krishna C. Penumatsa, PhD, Pulmonary, Critical Care and Sleep Division, Tufts Medical Center, 800 Washington Street, #257, Boston, MA 02111. Email: krishna.penumatsa@tuftsmedicine.org

This manuscript was sent to Erik B. Schelbert, MD, MS, Associate Editor, for review by expert referees, editorial decision, and final disposition.

Preprint posted on BioRxiv, December 17, 2023. doi: https://doi.org/10.1101/2023.12.15.571959.

Supplemental Material is available at https://www.ahajournals.org/doi/suppl/10.1161/JAHA.124.034363

For Sources of Funding and Disclosures, see page 12.

© 2024 The Author(s). Published on behalf of the American Heart Association, Inc., by Wiley. This is an open access article under the terms of the Creative Commons Attribution-NonCommercial-NoDerivs License, which permits use and distribution in any medium, provided the original work is properly cited, the use is non-commercial and no modifications or adaptations are made.

JAHA is available at: www.ahajournals.org/journal/jaha

RESEARCH PERSPECTIVE

What Is New?

- For the first time, we investigated whether cardiac and pulmonary tissue remodeling could be quantitatively assessed through a single imaging session using targeted molecular positron emission tomography and magnetic resonance imaging probes.
- Our studies show that collagen-targeted positron emission tomography and allysine-targeted molecular magnetic resonance imaging provide significantly elevated signal enhancement in an accelerated-aging-prone mouse model that underwent transverse aortic constriction surgery, which corresponded with pressure-volume loop measurements, echocardiography, histopathology, quantitative real-time polymerase chain reaction, and biochemical assay measurements.

What Question Should Be Addressed Next?

- Future studies are needed to test the validity of the dual molecular positron emission tomography—magnetic resonance imaging protocol for assessing cardiopulmonary fibrogenic progression and treatment response.

Nonstandard Abbreviations and Acronyms

%ID/cc	percent injected dose per cubic centimeter of tissue
%SI	percent signal increase
CBP8	type I collagen–targeted positron emission tomography probe
FLASH	fast low-angle shot
Gd-1,4	allysine-targeted fibrogenesis magnetic resonance probe
ID	injected dose
LL	left lung
LMR	lung-to-muscle ratio
LOX	lysyl oxidases
PH	pulmonary hypertension
PV	pressure–volume
RL	right lung
SAMP8	senescence-accelerated prone
SI	signal intensity
TAC	transverse aortic constriction
UTE	ultrashort echo time
VOI	volume of interest

Left ventricular (LV) compliance declines with age, which may contribute to an increased risk of heart failure in the elderly.[1,2] Pulmonary hypertension (PH), defined as an elevation of blood pressure in the pulmonary artery,[3,4] is a common comorbidity of left ventricular dysfunction leading to right ventricular failure,[5,6] cardiopulmonary remodeling,[7] and fibrosis.[8,9]

Multiple tests aid in diagnosing cardiopulmonary disease severity and progression, including echocardiogram,[10,11] magnetic resonance imaging (MRI),[12,13] and right heart catheterization.[14] However, at the time of diagnosis, the disease has often progressed to an advanced stage, where cardiac function has declined and cardiopulmonary fibrosis has developed.[15,16] It remains a challenge to detect the early onset of cardiopulmonary fibrosis and measure disease activity/fibrogenesis. The ability to diagnose LV dysfunction and PH at an early stage of the disease would allow for earlier initiation of therapy and potentially improved prognosis.[17,18]

Tissue fibrosis and stiffness, including that of the pulmonary vasculature and the heart, occur with PH,[19,20] cardiac overload syndromes,[21] and aging.[19,20] In response to elevated systemic arterial pressure, both the heart and lungs compensate to maintain homeostasis and subsequently undergo tissue remodeling, where myofibroblasts become activated and secrete inflammatory mediators and synthesize extracellular matrix components, including collagen proteins.[22] During this process of fibrogenesis, lysyl oxidases (LOXs) are upregulated and oxidize collagen lysine residues to the aldehyde allysine, which then undergoes condensation reactions with other collagen side chains to ultimately result in stable cross-links. An excess amount of extracellular matrix and extracellular matrix cross-linking leads to tissue stiffness and can ultimately lead to heart failure.[23]

We previously reported a type I collagen-targeted positron emission tomography (PET) probe (^{68}Ga-CBP8) and showed that ^{68}Ga-CBP8 PET could detect and stage pulmonary fibrosis in different mouse models of lung injury and in patients with idiopathic pulmonary fibrosis.[19,20,24,25] Collagen increases with increasing disease, and molecular imaging of collagen provides an overall assessment of fibrotic burden. We also showed that fibrogenesis (fibrotic disease activity), independent of overall fibrotic burden, could be noninvasively measured using a molecular MR probe targeted to allysine in animal models of lung, liver, and kidney fibrosis.[26–34] Allysine is present at high concentrations during fibrogenesis but is rapidly consumed by cross-linking reactions once the fibrosis-causing insult is removed. Allysine-targeted fibrogenesis magnetic resonance probe (Gd-1,4) is a recently described molecular MR probe that targets pairs of allysine residues and has improved sensitivity and dynamic range compared with earlier allysine-targeted probes.[29]

The advent of simultaneous PET–MRI allows 3-dimensional imaging of deep tissue structures to provide combined molecular, functional, and anatomic information. We hypothesized that both cardiac and pulmonary tissue remodeling could be quantitatively assessed through a single imaging session using appropriate molecular probes. Here, we sought to develop a dual molecular PET-MRI protocol to detect both cardiopulmonary fibrosis and fibrotic disease activity in an LV dysfunction model using collagen-targeted ^{68}Ga-CBP8 PET and allysine-targeted Gd-1,4 enhanced MRI in a single imaging session. To validate cardiopulmonary tissue remodeling, we conducted tissue characterization studies including histology, immunohistochemistry, quantitative real-time polymerase chain reaction, and biochemical assays. LV structure and biventricular function were assessed by echocardiography and pressure–volume (PV) loop.

METHODS

Data Availability

The data that support the findings of this study are available upon request from the corresponding authors.

Study Design

Six- to 7-month-old aging mouse models, SAMP8 mice, were used in this study. LV dysfunction was induced by left thoracotomy transverse aortic constriction (TAC) surgery using a 25-gauge needle in SAMP8 mice (Figure 1A) as described previously.[35] The TAC surgical procedure is provided in Data S1. Control mice received sham surgery. Mice were assigned to each study group (sham, TAC) by simple randomization. All animal experiments were handled in accordance with the US National Institutes of Health's *Guide for the Care and Use of Laboratory Animals* and in compliance with the Animal Research: Reporting of In Vivo Experiments guidelines.[36] All procedures were approved by the Tufts Medical Center and Massachusetts General Hospital Institutional Animal Care and Use Committees. A total of 81 sham (n=10 female, n=33 male) and TAC (n=6 female, n=32 male) mice were used in this study. The experimental design flowchart and exclusion criteria are provided in Figure S1. All experimental evaluations were performed in a nonblinded fashion except for the histopathological and echocardiography analysis. Sample sizes and statistical results are provided in the figure legends.

PV Loop Measurements

At 3 weeks after surgery, invasive PV loop measurements were recorded in isoflurane (1%–1.5%) anesthetized mice in the supine position as previously described.[35] Briefly, a PV catheter (Millar Instruments, Houston, TX) was inserted into the left ventricle (via carotid artery and aorta [preconstriction], sham [n=3 male], TAC [n=3 male]) or right ventricle (via jugular vein and right atrium, sham [n=6 male], TAC [n=4 male]) using a closed-chest approach as described previously.[21] PV loop data were analyzed using a LabChart application (AD Instruments, Dunedin, New Zealand). Animals were then euthanized using pentobarbital injection (120 mg/kg, intraperitoneal injection), and the lungs and hearts were inflated for histological preparation.

Echocardiography

Cardiac function and architecture were assessed using transthoracic echocardiography on anesthetized mice (sham [n=3 male], TAC [n=4 male]) using a Vevo2100 equipped with 9–18 MHz transducer (Visualsonics Inc., Toronto, Ontario, Canada). Once the left ventricle was clearly visualized, LV end-systolic and end-diastolic dimensions (M-mode) were measured, and the LV fractional shortening percentage and ejection fraction were calculated as previously described.[35] LV geometry was assessed using LV weights, LV posterior wall thickness, and volume during diastole. Blinded investigators performed echocardiography assessments on the day before surgery and 3 weeks after surgery.

Molecular Probes

^{68}Ga-CBP8 is a peptide-based PET probe targeting type I collagen, with a dissociation constant of 2.1±0.1 μM for type I human collagen and 4.6±0.5 μM for rat collagen (reported as mean±SD).[19] ^{68}Ga-CBP8 was synthesized as previously reported,[19,20,25,37] with some modifications described in Data S1. Gd-1,4 is a dual binding fibrogenesis probe targeting allysine, with a relaxivity of 17.4±1.0 $mM^{-1}s^{-1}$ when bound to allysine containing protein at 1.41 T, 37 °C, and was synthesized as described (reported as mean±SD).[29]

Cardiothoracic PET-MRI

Mice (sham [n=7 female, n=9 male], TAC [n=6 female, n=13 male]) were imaged 3 weeks after surgery on a 4.7 T Bruker Biospec MRI equipped with a PET insert (Bruker, Billerica, MA). Mice were anesthetized with isoflurane (1%–2%). The body temperature was maintained at 37 °C, and inhaled isoflurane concentration was adjusted to maintain a respiration rate of 55 to 65 breaths per minute. The tail vein was cannulated for intravenous delivery of molecular probes.

^{68}Ga-CBP8 was intravenously administered with an injected dose between 18 and 34 MBq at a volume of 100 to 150 μL before the mouse was placed in the PET-MR scanner. Next, the mouse was placed

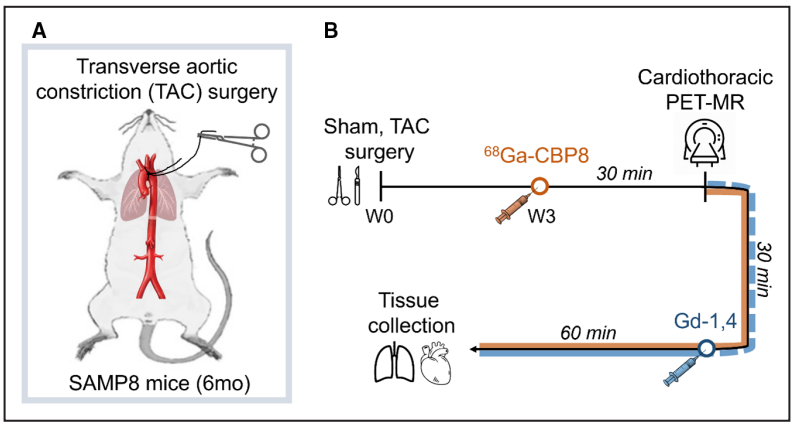

Figure 1. Study design.
A, Transverse aortic constriction (TAC; n=6 female, n=13 male) and sham (n=7 female, n=9 male) mice underwent cardiothoracic positron emission tomography–magnetic resonance imaging (PET-MRI) 3 weeks after surgery. **B**, Type I collagen–targeted PET probe (^{68}Ga-CBP8) was intravenously administered with an injected dose between 18 and 34 MBq at a volume of 100 to 150 μL before the mouse was placed in the PET-MRI scanner. PET (solid orange line) and preinjection MRI (dashed blue line) scans were acquired for 30 min followed by administration of allysine-targeted fibrogenesis MR probe (Gd-1,4) (100 μmol/kg, 75–110 μL). Cardiothoracic MRI sequences (2-dimensional T1-weighted fast low-angle shot [FLASH], and 3-dimensional ultrashort echo time [UTE]) were repeated for a period of 60 min after injection (solid blue line). Afterward, each mouse was euthanized, and lung and heart tissue were collected for analysis.

in the scanner, and PET-MRI was acquired simultaneously (Figure 1B). Preinjection MRI scans were acquired for 30 minutes and encompassed cardiac/respiratory gated 2-dimensional T1-weighted fast low-angle shot (FLASH): repetition time/echo time/inversion time=609.5/3.5/590 ms, number of averages=3, bandwidth=390.6 Hz/pixel, flip angle=50°, field of view =40×40 mm^2, matrix size=200×200, slice thickness=1 mm, acquisition time=6:05 minutes; 3-dimensional ultrashort echo time (UTE): repetition time/ echo time =4/0.012 ms, number of averages=1, bandwidth=976.6 Hz/pixel, flip angle=16°, field of view=32×32×32 mm^3, matrix size=128×128×128, acquisition time=3:25 minutes; and 3-dimensional FLASH: repetition time/echo time =15/2.5 ms, number of averages=4, bandwidth=1250 Hz/pixel, flip angle=12°, field of view=27.5×48×24 mm^3, matrix size=60×120×60, acquisition time=3:36 minutes. Then Gd-1,4 was administered (100 μmol/kg, 75–110 μL) followed by 2-dimensional FLASH and 3-dimensional UTE MRI, which were repeated for a period of 60 minutes.

After the PET-MRI session, each mouse was euthanized followed by tissue collection. The left lung (LL), right lung (RL), muscle, liver, kidney, blood, and tail were collected from all animals. Additionally, the heart was separated into 3 parts: right ventricle, septum, and left ventricle. All tissue samples were weighed, followed by measuring the radioactivity with a γ counter (Wizard2Auto Gamma, PerkinElmer). Biodistribution measurements (sham [n=2 female, n=8 male], TAC [n=1 female, n=7 male]) were calculated on the basis of injected dose (ID), decay-corrected, and presented as %ID/g for all organs. Lung measurements were reported as %ID/lung.

PET Image Analysis

The PET data sets were reconstructed using the maximum a posteriori probability (0.5 mm) algorithm run over 10 iterations to a voxel size of 0.5×0.5×0.5 mm^3. PET data were reconstructed in 6×5-minute frames and 3×10-minute frames. Radioactivity measurements were performed on averaged PET frames from 65 to 95 minutes after injection.

Reconstructed PET-MR data were quantitatively evaluated using the AMIDE software package.[38] MR images (3D FLASH and UTE) were used to draw volumes of interest (VOIs) over the following organs: LL, RL, and myocardium (septal and anterior wall of the left ventricle). An additional two VOIs were drawn on the left and right forelimb muscles. The VOIs were applied to decay-corrected PET scans. Radioactivity measurements were converted to counts per milliliter per minute and then divided by the ID to obtain an imaging VOI-derived percentage of the injected radioactive dose per cubic centimeter (%ID/cc). PET measurements were also reported as the ratio of tissue signal (lung [LMR] or myocardium) to muscle.

MRI Analysis

For cardiac 2-dimensional FLASH images, a region of interest was manually drawn in ImageJ (Fiji, version 1.0) and encompassed the septal and anterior walls of the left ventricle while avoiding the blood pool. A second region of interest was placed on the phantom doped with Dotarem (gadoterate meglumine) to normalize the signal intensity across all the 2-dimensional FLASH images. Myocardial signal intensity (SI) was measured in each normalized 2-dimensional FLASH image. SI from preinjection images (n=3) were averaged. %SI increase was calculated by subtracting the preinjection SI from the postinjection SI and then dividing by the preinjection SI (as shown in Equation 1).

$$\%\,\text{SI increase} = \left(\text{SI}_{\text{post}} - \text{SI}_{\text{pre}}\right) / \text{SI}_{\text{pre}} \quad (1)$$

Pulmonary 3-dimensional UTE images were normalized to the SI of a Dotarem (gadoterate meglumine) doped phantom placed next to the animals during image acquisition. VOI measurements included LL, RL, and muscle. LMR was calculated by dividing the SI in the lungs by the SI of the forelimb triceps muscle (as shown in Equation 2) as performed in previous pulmonary disease studies.[27,34] LMR from preinjection scans (n=3) were averaged. LMR from RL and LL VOIs were averaged for each UTE image.

Change in LMR was calculated by subtracting the preinjection LMR from the postinjection LMR (as shown in Equation 3). In addition, pulmonary %SI increase was computed from 3-dimensional UTE images using (as shown in Equation 1).

$$\text{LMR} = \text{lung to muscle ratio} = \text{SI}_{\text{lung}} / \text{SI}_{\text{muscle}} \quad (2)$$

$$\Delta\text{LMR} = \text{LMR}_{\text{post}} - \text{LMR}_{\text{pre}} \quad (3)$$

%SI increase and change in LMR were averaged 20–45 minutes after injection of the Gd-1,4 probe, and dynamic curves are shown in Data S1. Change in pulmonary tissue to change in muscle contrast-to-noise ratio was computed from the pre- and postinjection MR images as described in Data S1.

Histology and Immunohistochemistry

A subset of cardiac (sham [n=5 male], TAC [n=8 male]) and pulmonary (sham [n=4 male], TAC [n=6 male]) tissue samples was fixed with 4% formaldehyde, paraffin-embedded, and sliced at 5 μm thickness. Cardiac samples were cut in the short axis at the midventricle and lung samples were inflated before embedding. Trichrome staining was performed by the Specialized Histopathology Services–Massachusetts General Hospital Core using standard methods.

LOX and transglutaminase protein expressions in the lung and heart tissues were detected using immunohistochemistry assays with antibodies against LOX (1:250; NB100-2527, Novus Biologicals) and transglutaminase (1:250; ab421, Abcam; protocol provided in Data S1).

The slides were scanned using NanoZoomer Slide Scanner (Hamamatsu) at ×20 original magnification. For cardiac tissue samples, the percentage of fibrosis was measured from Trichome slides using ImageJ (Fiji, version 1.0) with a uniform color threshold segmentation approach.[39,40] The percentage of fibrosis was computed with respect to the area of the left ventricle. For pulmonary tissue samples, the regions of fibrosis and disease classification (mild, moderate, severe) were determined by an experienced pulmonary pathologist (L.P.H.).

RNA Isolation and Quantitative *Real-Time Polymerase Chain Reaction*

Quantitative real-time polymerase chain reaction (PCR) was performed to measure the gene expression in collagen, type 1, α1 (*Col1a1*), and lysyl oxidase (*LOX-1*, *LOX-2*, *LOX-3*, *LOX-4*) as demonstrated in previous mouse models.[33] To isolate RNA and conduct quantitative real-time PCR, frozen heart and lung tissues were used (sham [n=8 male], TAC [n=8 male]). The RNA extraction was performed using TRIzol (Invitrogen) according to the manufacturer's instructions. In summary, 1 μg of extracted RNA was reverse transcribed using a High-Capacity cDNA Reverse Transcription Kit.

During the real-time PCR, the Applied Biosystems TaqMan Gene Expression Master Mix was used with predeveloped primer/probe assays from Thermo Fisher Scientific for *Col1a1* (Mm0080166-g1), *LOX-1* (Mm 00495386_m1), *LOX-2* (Mm00804739_m1), *LOX-3* (Mm 01184865_m1), *LOX-4* (Mm 00446385_m1) and 18S ribosomal RNA primer/probe set (Hs 03003631; Thermo Fisher Scientific).

For fibronectin, real-time PCR analysis was performed using 2x SYBR Green Master Mix (Thermo Fisher Scientific) on an ABI Prism 7900 Sequence Detection System (Thermo Fisher Scientific) as described previously.[41] Human- and mouse-specific primer sets (IDT Technologies, Coralville, IA) were used.

To normalize the cycle threshold values, 18s ribosomal RNA levels were used. The relative quantification of specific genes was determined using the ΔΔcycle threshold method as previously described.[41,42]

Biochemical Determination of Hydroxyproline and Allysine

Hydroxyproline in the left ventricle (sham [n=10 female, n=14 male]), (TAC [n=6 female, n=12 male]) and

RL (sham [n=10 female, n=14 male], TAC [n=6 female, n=12 male]) was measured with high-performance liquid chromatography following a published method.[43] Allysine of the septum (sham [n=3 female, n=2 male], TAC [n=3 female, n=2 male]) and LL (sham [n=9 female, n=13 male], TAC [n=6 female, n=12 male]) was quantified using high-performance liquid chromatography following a published method.[34,44] Measurements are reported as amounts per wet weight of tissue (g) or amounts per lung.

Statistical Analysis

Quantitative measurements are displayed as box plots. The bottom and top of the box represent the first and third quartiles, the center band is the mean, the whiskers report the minimum and maximum values, and individual values are displayed as points on the plot. Measurements are reported as mean±SEM, unless noted otherwise, and significant differences are reported when $P<0.05$. The Kolmogorov–Smirnov test was used to assess normality in each data set and an F-test was used to compare variances. If the data sets had a normal distribution and equal variances an unpaired 2-tailed *t* test was used to compare differences between the 2 groups (sham, TAC). If the data sets had a normal distribution and unequal variances, an unpaired 2-tailed *t* test with Welch's correction was performed. If the data sets did not have a normal distribution, a Mann–Whitney test was performed. Linear associations were investigated using a simple linear regression. All statistical analyses were performed in GraphPad Prism 9.0 (GraphPad Software, La Jolla, CA).

RESULTS

In the heart, trichrome staining showed myocardial interstitial fibrosis in TAC mice (Figure 2A), which corresponded to a significant increase in percentage of fibrotic area with respect to the LV area compared with sham mice (1.6±0.1% [sham, n=5] versus 4.8±0.7% [TAC, n=8]; $P=0.006$; Figure 2B). Hydroxyproline, a measure of total collagen and marker of fibrosis, was significantly elevated in the myocardium of TAC mice (400±20 [sham, n=24], 555±20 [TAC, n=18] μg/g; $P<0.0001$; Figure 2C). Allysine, a marker of fibrogenesis, was significantly elevated in the myocardium of TAC mice (13±2 [sham, n=5] versus 22±2 [TAC, n=5] nmol/g; $P=0.02$; Figure 2D). Gene expression of proteins associated with fibrogenesis: collagen type 1, α 1 (*Col1a1*), and lysyl oxidase paralogs *LOX-1, LOX-2, LOX-3*, and *LOX-4*, showed that these were all significantly elevated in the LV myocardium of TAC mice compared with sham ($P<0.05$; Figure 2E). In addition, *Col1a1* and *LOX-4* expression in the right ventricular myocardium was significantly elevated in TAC mice (Figure S2A). Histopathology of pulmonary tissue showed heterogeneity of disease. Half of the TAC mice (3/6) had moderate to severe lung injury, while the other half had mild lung injury (Figure 3A). Lung injury was not detected in sham mice (Figure 3A). TAC mice with moderate to severe disease showed several histopathological findings of acute lung injury and tissue remodeling including (1) inflammation, (2) focal regions of fibrosis surrounding blood vessels and airways, (3) presence of hemosiderin and hemosiderosis, and (4) leaked fibronectin into the extracellular space. LOX and transglutaminase staining were present predominantly around pulmonary blood vessels indicating active tissue remodeling and distribution of LOX and transglutaminase proteins (Figure 3A). Focal regions of fibrotic activity led to a moderate but significant elevation in hydroxyproline of the whole RL (143±6 [sham, n=24], 189±15 [TAC, n=18] μg/lung; $P<0.01$; Figure 3B) of TAC mice compared with sham. Allysine in the whole LL (5.8±1 [sham, n=17], 7.5±1 [TAC, n=16] nmol/lung; $P=0.17$; Figure 3C) was elevated in TAC mice, but this elevation was not statistically significant. However, RT-qPCR uncovered significantly elevated *Col1a1, LOX-2, LOX-3*, and *LOX-4* gene expression in the lungs ($P<0.05$; Figure 3D). Additionally, TAC mice had significantly lower body weight with a significant elevation of right ventricular weight to body weight and lung weight to body weight, compared with sham mice indicating cardiopulmonary disease progression (Figure S2B through S2E).

Echocardiographic (Table 1, Figure S3) and invasive hemodynamic PV loop (Table 2) measurements were collected to assess LV remodeling and PH secondary to LV dysfunction in the TAC mice. Echocardiographic M-mode measurements showed signs of LV hypertrophy, including increases in LV weight ($P=0.008$), internal diameter at end-diastole ($P=0.008$) and end-systole ($P=0.017$), posterior wall thickness ($P=0.037$), and volume ($P=0.009$) at end-diastole in TAC mice. In addition, echocardiographic data showed LV ejection fraction ($P=0.008$) and fractional shortening ($P=0.006$) were significantly reduced, demonstrating TAC surgery induced LV systolic dysfunction. PV loop functional analysis also identified markers of LV dysfunction including significantly elevated aortic systolic ($P=0.005$) and LV end-diastolic ($P=0.011$) pressures as well as reduced aortic diastolic pressure ($P=0.007$), cardiac output ($P=0.003$), stroke volume ($P=0.004$), and stroke work ($P=0.036$) in TAC mice. Effective arterial elastance, a measure of arterial load, was significantly elevated in TAC mice ($P=0.012$). Right ventricular systolic pressure was significantly elevated to 42.8±6.4 mm Hg in TAC mice compared with 22.8±1.8 mm Hg in sham mice ($P=0.006$), indicative of PH in the TAC mice.

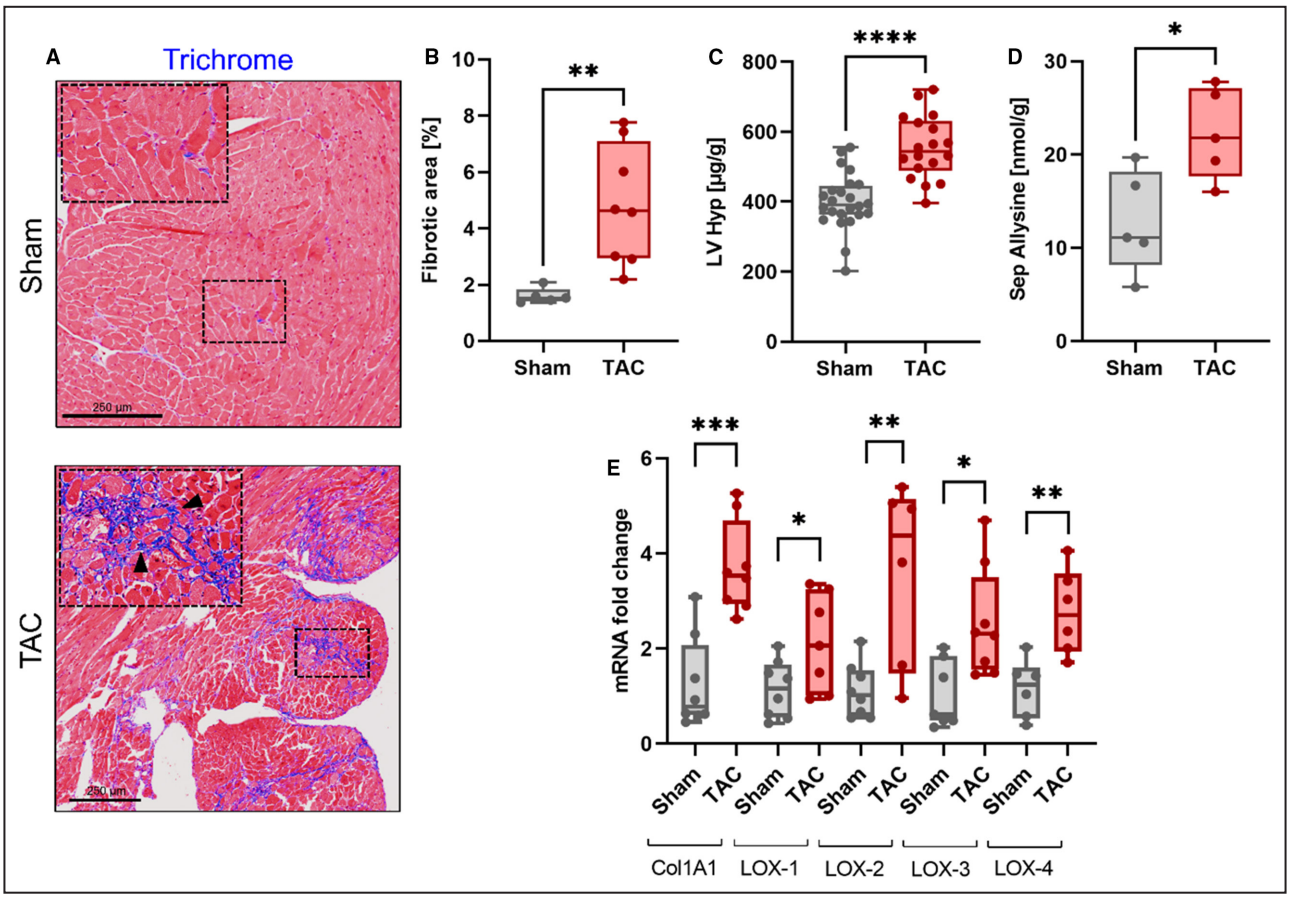

Figure 2. Heart tissue characterization.
A, Representative trichrome staining of the myocardium shows regions of interstitial fibrosis in transverse aortic constriction (TAC) senescence-accelerated prone (SAMP8) mice (inset, arrowheads). **B**, The percentage of trichrome fibrosis-positive tissue with respect to the left ventricular area of the short-axis slice (n=5 [sham], n=8 [TAC]). **C**, Hydroxyproline (Hyp) content as a marker of myocardial fibrosis in sham (n=24) and TAC (n=18) mice. **D**, Allysine content as a marker of myocardial fibrogenesis measured in the septum (Sep) of sham and TAC mice (n=5 per group). **E**, Gene expression levels of collagen, type 1, α 1 (*Col1a1*) and lysyl oxidases (*LOX-1*, *LOX-2*, *LOX-3*, *LOX-4*) in sham and TAC SAMP8 mice (n=8 [sham], n=8 [TAC]). Fold changes were normalized with housekeeping gene (18s). **P*<0.05, ***P*<0.01, ****P*<0.001, and *****P*<0.0001.

MRI and PET were simultaneously acquired in the heart and lungs (Figure 4A, 4B and 5A, 5B; Figures S4 through S9). MRI %SI increase in the myocardium was significantly elevated in TAC mice (29±4% [TAC, n=19] versus 6.1±1% [sham, n=14]; *P*<0.0001; Figure 4C, Figure S4B). ^{68}Ga-CBP8 PET showed a significant increase in radioactivity in the myocardium of TAC mice (1.6±0.2 [TAC, n=10] versus 0.7±0.1 [sham, n=10] %ID/cc, *P*=0.003; Figure 4D). In addition, the myocardium-to-muscle ratio PET values were significantly elevated (1.8±0.1 [TAC, n=10] versus 1.6±0.1 [sham, n=10]; *P*=0.02) 65 to 95 minutes after injection of ^{68}Ga-CBP8 (Figure 4E; Figures S7 and S8B).

From UTE MR imaging of the lungs, TAC mice showed a significantly higher mean pulmonary %SI increase (87±12 [TAC, n=18] versus 20±3 [sham, n=14]; *P*<0.0001) and ΔLMR (0.3±0.03 [TAC, n=18] versus 0.08±0.01 [sham, n=14]; *P*<0.0001) at 20 to 45 minutes after injection of Gd-1,4 (Figure 5C and 5D, Figure S5B). In addition, the lungs of TAC mice had a significant increase in preinjection contrast-to-noise and LMR (Figure S6A and S6B). The change in contrast-to-noise ratio from pre- and postinjection imaging was significantly elevated in the lungs of TAC mice (Figure S5C, S6C and S6D). ^{68}Ga-CBP8 PET showed a significant increase in lung radioactivity of TAC mice (1.3±0.2 [TAC, n=10] versus 0.5±0.1 [sham, n=10] %ID/cc; *P*=0.003) and the ratio of LMR PET values were significantly increased (1.5±0.04 [TAC, n=10] versus 1.2±0.04 [sham, n=10]; *P*<0.001) 65 to 95 minutes after injection of ^{68}Ga-CBP8 (Figure 5E and 5F; Figures S7 and S8C). There were no differences in MRI or PET measurements between RL and LL (Figures S6C and S9). Ex vivo biodistribution studies showed significantly increased activity in the heart and lungs of TAC mice (Figure S10A and S10B) that was linearly associated with in vivo PET measurements (heart: 1.0 %ID/cc [PET] per %ID/g [biodistribution], R^2=0.98, *P*<0.0001;

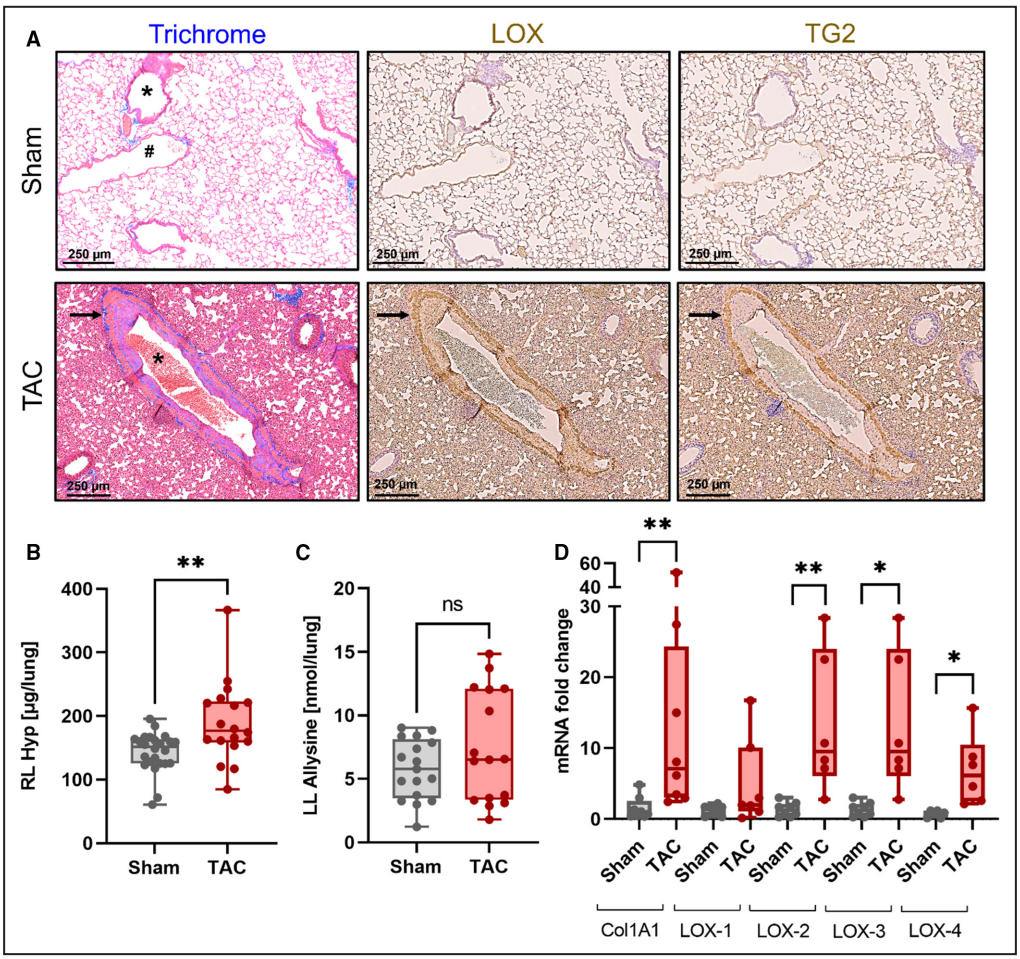

Figure 3. Lung tissue characterization.
A, Representative histology, and immunohistochemistry images show vessel remodeling (arrows) through fibrosis (trichrome)-positive, lysyl oxidase (LOX)-positive, and transglutaminase (TG2)-positive regions in the lungs of transverse aortic constriction (TAC) senescence-accelerated prone (SAMP8) mice. Sham mice did not exhibit vessel remodeling. Pulmonary vessels (*), airways (#). **B**, Hydroxyproline (Hyp) content as a marker of pulmonary fibrosis measured in the right lung (RL) of sham and TAC mice (n=24 [sham], n=18 [TAC]). **C**, Allysine content as a marker of pulmonary fibrogenesis measured in the left lung (LL) of sham and TAC mice (n=17 [sham], n=16 [TAC]). **D**, Gene expression levels of collagen, type 1, α1 (*Col1a1*), and lysyl oxidases (*LOX-1*, *LOX-2*, *LOX-3*, *LOX-4*) in the lungs of sham and TAC SAMP8 mice (n=8 [sham], n=8 [TAC]). Fold changes were normalized with housekeeping gene (18s). *P<0.05, and **P<0.01; ns, not significant.

lung: 0.29 %ID/cc [PET] per %ID/g [biodistribution], R^2=048, P=0.004; Figure S10C,D).

DISCUSSION

Clinical prevalence of LV dysfunction with heart failure increases with aging.[45,46] If left untreated, the associated elevated pressure overload in the pulmonary circulation can progress to secondary PH and right ventricular failure with poor clinical outcomes.[8,9] Physiologic responses to aging-related cardiac pressure overload have been linked to structure–function abnormalities associated with fibrogenic remodeling leading to decreased tissue compliance and LV dysfunction.[47,48] However, there is a lack of sensitive noninvasive tools available to assess the extent of fibrosis and early onset of disease. Previous studies from our lab and others have shown that SAMP8, a mouse model of aging, and TAC-induced LV pressure overload mouse model developed cardiac and pulmonary fibrosis and PH associated with LV dysfunction.[8,9,41,49]

In consideration of the common pathophysiological features of aging and pressure overload, we have now analyzed if TAC-induced pressure overload in an aging mouse model exacerbates the fibrogenic remodeling in lung and heart tissues. Here, we further proposed a dual imaging modality (PET-MRI) to image at a systems

Table 1. Echocardiographic Assessment of Left Ventricular Structure and Function

Measurement	Sham (n=3)	TAC (n=4)	*P* value*
LV weights (mg)	125±10	260±27	0.009**
LVIDd (mm)	3.3±0.2	4.3±0.2	0.008**
LVIDs (mm)	2.0±0.4	3.5±0.2	0.017*
LVPWd (mm)	1.1±0.1	1.5±0.1	0.037*
LV Vol;d (uL)	43.7±6.2	82.7±6.8	0.009**
EF (%)	60±2	40±4	0.008**
FS (%)	31±1	19±2	0.006**

All data are shown as means±SEM.

EF indicates ejection fraction; FS, fractional shortening; LV, left ventricular; LV Vol;d, left ventricular volume during diastole; left ventricular internal diameter at end-diastole; LVIDs, left ventricular internal diameter at end-systole; and LVPWd, left ventricular posterior wall thickness at end-diastole.

*P<0.05;

**P<0.01.

level (both heart and lungs) of disease in a model with pulmonary and cardiac injury using 2 imaging probes that targeted type 1 collagen (^{68}Ga-CBP8) or allysine (Gd-1,4).

Fibrosis is a common response to injury and characterized by excess deposition of collagens, primarily type I collagen. Both the amount of fibrosis and whether the disease is ongoing are important clinical questions. Previous studies showcase that the PET probe, ^{68}Ga-CBP8, and its MRI analog, EP-3533, can detect type 1 collagen and stage disease in preclinical models of pulmonary,[19,20,50] cardiac,[51,52] and hepatic[53–55] fibrosis. Both probes, ^{68}Ga-CBP8 and EP-3533, have been extensively validated through blocking experiments, comparison to control probes, and gain/loss of function models. The MRI probe, Gd-1,4, has its own unique target, allysine, and allysine-targeted MRI has been employed to detect fibrogenesis in models of lung, liver, and kidney fibrosis.[26–33] Both probes, ^{68}Ga-CBP8 and Gd-1,4, do not interfere with one another and were able to detect focal regions of fibrosis and disease activity in the heart and lungs.

Table 2. Hemodynamic PV Loop Measurements

PV loop measurements	Sham	TAC	*P* value*
Left ventricle	n=3	n=3	
Aortic systolic pressure, mm Hg	69.3±0.7	84.3±2.7	0.005**
Aortic diastolic pressure, mm Hg	52±4.0	24.6±3.7	0.007**
LVEDP, mm Hg	3.3±1.5	12.3±1.5	0.011*
Max dP/dt, mm Hg/s	4113±92	2676±529	0.055
Effective arterial elastance, mm Hg/μL	3.3±0.3	8.6±1.2	0.012*
Stroke volume, μL	21.6±1.9	8.3±1.5	0.004**
Stroke work, μL×mm Hg	1117±223	357±107	0.037*
Cardiac output, mL/min	9.0±0.7	3.3±0.5	0.003**
Heart rate, beats/min	417±28	390±34	0.573
Right ventricle	(n=6)	(n=4)	
RV systolic pressure, mm Hg	22.8±1.8	42.8±6.4	0.006**

All data are shown as means±SEM.

LV indicates left ventricular; LVEDP, left ventricular end-diastolic pressure; Max dP/dt, maximum rate of pressure change in the left ventricle; PV, pressure–volume; and RV, right ventricular.

*P<0.05;

**P<0.01.

Despite the milder form of TAC (25-gauge) in the senescence-accelerated mice,[35] allysine biochemical assay, and LOX immunohistochemistry demonstrated evidence of active fibrosis in the heart and lungs, which corresponded to imaging findings. The SAMP8 TAC mice had focal regions of pulmonary fibrosis surrounding arteries and airways, which is a characteristic of PH tissue remodeling.[56–58] Of note, we previously reported that a profibrogenic crosslinking enzyme, tissue transglutaminase, was elevated in a pressure-overloaded TAC[41] and a senescent-prone mouse model of aging[49] where myocardial fibrosis and heart failure with preserved ejection fraction have been described. We also identified that elevation of transglutaminase activity is causative for fibrogenic remodeling, including collagen deposition in experimental mouse models of cardiopulmonary fibrosis.[41] Consistent with these findings, using immunohistochemical imaging, we now for the first time show that TAC surgery induced transglutaminase expression in both pulmonary arteries and airways (Figure 3A). Taken together, assisted by novel biochemical and imaging methods, the study further supports that SAMP8 TAC mice show signs of tissue fibrogenic remodeling in the heart and lungs at an advanced stage of heart failure.

In the clinic, cardiovascular MRI techniques like late gadolinium enhancement[59–61] and extracellular volume mapping[62,63] provide an indirect measurement of collagen deposition in the heart, but do not provide an assessment of disease activity or pulmonary fibrosis. Pulmonary hypertension is diagnosed by right heart catheterization to measure pulmonary arterial pressures. Here, we were able to detect both fibrosis and fibrogenesis in the heart and lungs noninvasively in a mouse model that resulted in a mild and heterogeneous disease of LV dysfunction and secondary PH. The dual molecular PET-MR imaging protocol described here has the potential to stage cardiopulmonary disease, provide early diagnosis of disease activity, and monitor treatment response.

There are some limitations to the study. The long aging period of the mice (6 months) in combination with a complex invasive surgical TAC procedure limited the number of experiments we could perform. Previous work investigated the sex differences of the TAC model and demonstrated that male mice develop increased disease severity.[64,65] Our initial studies showed the disease was more severe in male mice, and therefore,

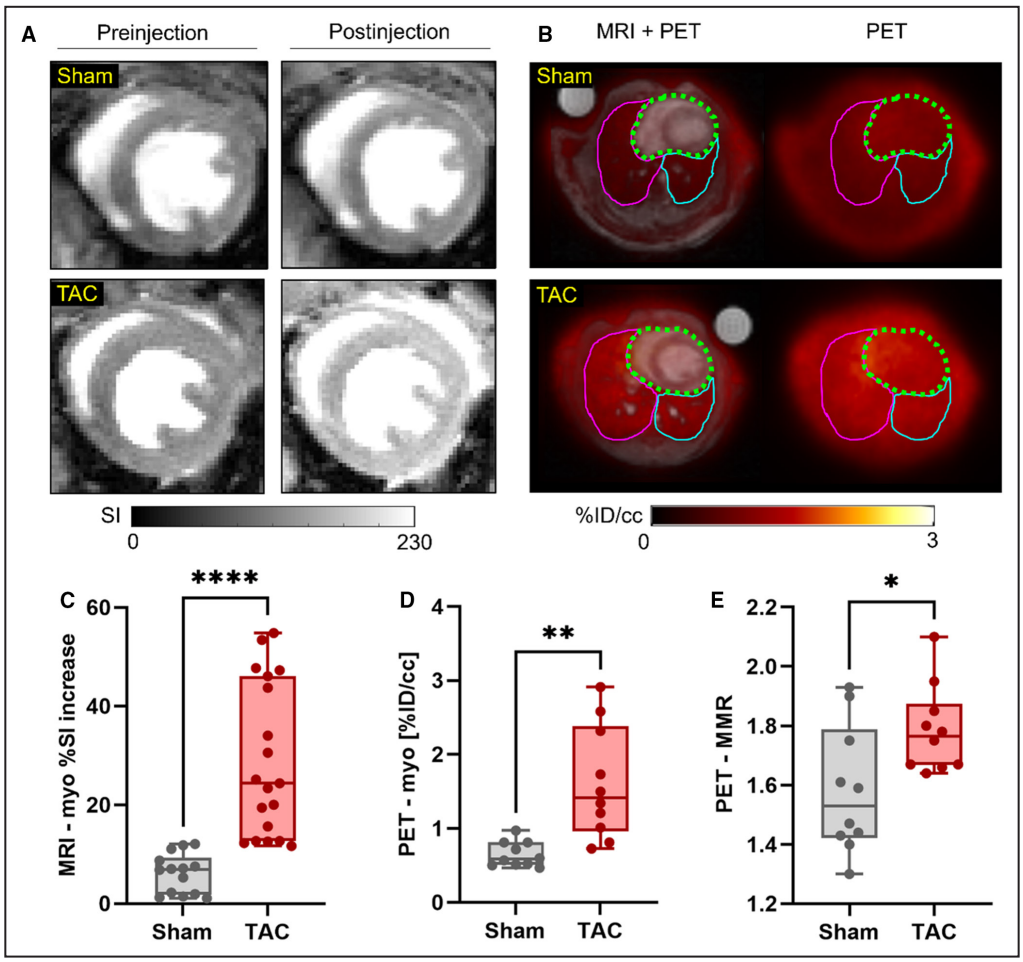

Figure 4. Heart imaging.
A, Short-axis myocardial 2-dimensional T1-weighted fast low-angle shot (FLASH) images from sham and transverse aortic constriction (TAC) mice before injection and 20 min after injection of allysine-targeted fibrogenesis magnetic resonance probe (Gd-1,4) (100 μmol/kg, intravenous injection). **B**, Axial positron emission tomography-magnetic resonance (PET-MR) fused images and PET-only images (heart: dashed green line, right lung [RL]: fuchsia solid line, left lung [LL]: blue solid line) from sham and TAC mice 86 min after injection of type I collagen–targeted PET probe (^{68}Ga-CBP8) (28 MBq, intravenous injection). **C**, Percent signal intensity increase (%SI) in the myocardium (myo) relative to preinjection images at 20 to 45 min after injection of Gd-1,4 (n=14 [sham], n=19 [TAC]). **D**, Myocardium; and **E**, myocardium-to-muscle PET signal ratio (MMR) 65–95 min after injection of ^{68}Ga-CBP8 (n=10 per group). *P<0.05, **P<0.01, and ****P<0.0001.

after initial experiments using both sexes, we focused the current study on male mice, which limits the generalizability of these results to females. Future studies would need to include detailed comparisons between the sexes. Second, we prioritized the specific binding probes during imaging studies. Ideally, negative control probes[19] would have been used in a subset of mice to validate that signal elevation was caused by specific binding of the imaging probe. However, extensive work was performed to establish the specific binding of the PET probe, ^{68}Ga-CBP8, in the lungs[19,20] and the specific binding of the MR-probe, Gd-1,4, in the liver.[29] Additionally, the fibrosis and fibrogenesis were validated through histology, RT-qPCR, and high-performance liquid chromatography biochemical measurements of hydroxyproline and allysine. Third, compared with clinical cardiothoracic MR, the sequences available on the small animal scanner require much longer acquisition times, which limited our imaging protocol to focus on molecular imaging. Extending this work to a human protocol would likely include established cardiovascular MR techniques, such as delayed gadolinium enhancement, T2 edema imaging, cardiac function, LV volumes, LV mass, and wall thickness measurements.

In conclusion, injection of collagen-targeted ^{68}Ga-CBP8 and allysine-targeted Gd-1,4 probes led to elevated PET and MRI signals, respectively, which correlated with fibrosis and fibrogenesis markers. To our knowledge, this is the first study to implement a dual molecular MRI and PET imaging protocol using 2

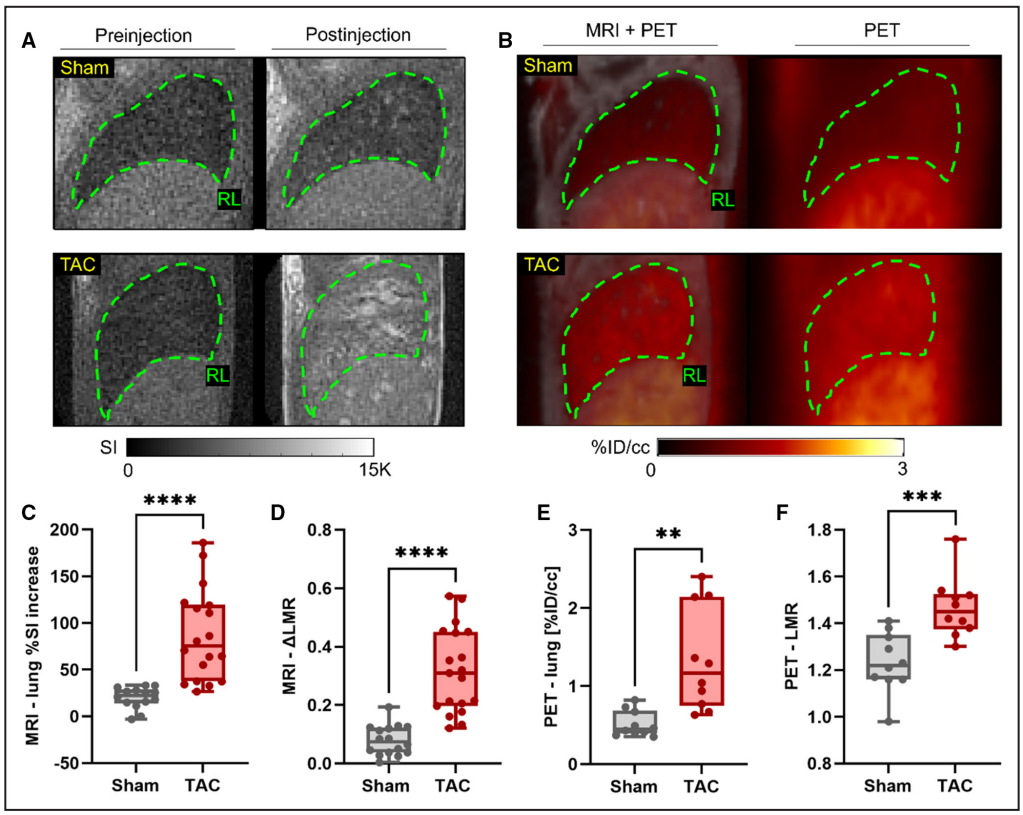

Figure 5. Lung imaging.
A, Sagittal 3-dimensional ultrashort echo time (UTE) images from sham and transverse aortic constriction (TAC) mice before injection and 20 to 45 min after injection of allysine-targeted fibrogenesis magnetic resonance probe (Gd-1,4) (100 μmol/kg, intravenous injection). **B**, Sagittal positron emission tomography–magnetic resonance (PET-MR) fused images and PET-only images (right lung [RL]: dashed green line) from sham and TAC mice 86 min after injection of type I collagen–targeted PET probe (^{68}Ga-CBP8) (28 MBq, intravenous injection). **C**, Percent signal intensity increase (%SI) and **D**, change in lung-to-muscle MRI signal ratio (ΔLMR) relative to preinjection images at 20 to 45 min after injection of Gd-1,4 (n=14 [sham], n=18 [TAC]). **E**, Lung; and **F**, lung-to-muscle PET signal ratio (LMR) 65 to 95 min after injection of ^{68}Ga-CBP8 (n=10 per group). $^{**}P<0.01$, $^{***}P<0.001$, and $^{****}P<0.0001$.

molecular probes to image 2 organs. Overall, the study demonstrates the potential to assess disease activity and burden at a systems level by characterizing heart and lung disease during a single imaging session. Future work will include a longitudinal study to assess disease progression and therapeutic response in a mouse model of aging-associated LV dysfunction and PH.

ARTICLE INFORMATION

Received March 7, 2024; accepted May 14, 2024.

Affiliations

Department of Radiology, Athinoula A. Martinos Center for Biomedical Imaging, Massachusetts General Hospital and Harvard Medical School, Boston, MA (B.F.M., I.Y.Z., Y.N., Y-C.C., M.L.F., S.S., H.M., J.W., N.R., A.T.B., S.E.Z., P.C.); Institute for Innovation in Imaging, Massachusetts General Hospital, Boston, MA (B.F.M., I.Y.Z., Y.N., M.L.F., S.S., H.M., N.R., A.T.B., S.E.Z., P.C.); Department of Medicine, Division of Cardiology, Massachusetts General Hospital and Harvard Medical School, Boston, MA (E.A.A.); Bruker BioSpin, Preclinical Imaging, Billerica, MA (C.M.S.); Department of Medicine, Division of Pulmonary and Critical Care Medicine, Massachusetts General Hospital and Harvard Medical School, Boston, MA (L.P.H., M.D.); Department of Pathology, Massachusetts General Hospital, Harvard Medical School, Boston, MA (L.P.H.); Pulmonary, Critical Care and Sleep Medicine, Tufts Medical Center, Boston, MA (Y.S., R.R.W., B.L.F., N.S.H., K.C.P.); and Molecular Cardiology Research Institute, Tufts Medical Center, Boston, MA (G.L.M., R.M.B.).

Acknowledgments

The authors greatly appreciate support from the Specialized Histopathology Services–Massachusetts General Hospital Core for histology staining.

Author Contributions: Study concept and design: Drs Moon, Zhou, Fanburg, Hill, Penumatsa, and Caravan; left thoracotomy transverse aortic constriction surgery: Drs Hill and Blanton, G. L. Martin and R. R. Warburton; pressure–volume loop experiments: G. L. Martin, R. R. Warburton and Drs Blanton and Penumatsa; echocardiography experiments: Drs Blanton and Penumatsa and R. R. Warburton; development and synthesis of molecular fibrogenesis MR-probe (Gd-1,4); Drs Ning and Akam; radiolabeling of type I collagen binding PET-probe (^{68}Ga-CBP8): Drs Le Fur, Shuvaev and Ma and S. E. Zygmont; animal preparation for imaging studies and probe injections: Dr Moon and J. Weigand-Whittier and N. Rotile; cardiothoracic PET-MRI acquisition and image processing: Drs Moon, Zhou, and Chen and C. M. Solsona, J. Weigand-Whittier, and N. Rotile; tissue collection, Dr Moon, R. R. Warburton, M. Drummond, and A. T. Boice; biodistribution measurements: Dr Moon, M. Drummond, and A. T. Boice; histology and immunohistochemistry: Drs Hariri, Moon, Sharma, and Penumatsa and R. R. Warburton; RNA isolation and quantitative reverse transcription polymerase chain reaction: Drs Sharma and Penumatsa and R. R. Warburton; biochemical assays: Drs

Moon, Le Fur, Shuvaev, Akam, and Ma, and M. Drummond; statistical analysis, all authors; manuscript drafting and editing for important intellectual content, all authors; and approval of final version of submitted manuscript, all authors.

Sources of Funding

This work was supported by grants from the National Institutes of Health to Dr Penumatsa (R01AG064064), to Dr Caravan (R33HL154125, R01HL153606, R01DK121789, R01DK121789-S1, OD028499, OD032138, OD025234, and OD023503), to Dr Blanton (R01HL162919) and by the Tupper Research Fund at Tufts Medical Center (Dr Penumatsa).

Disclosures

Drs Ning, Akam, Ma, and Caravan are inventors of a filed patent based on the work here (Molecular probes for in vivo detection of aldehydes; PCT/US2022/072310). Dr Caravan has equity in and is a consultant to Collagen Medical LLC, has equity in Reveal Pharmaceuticals Inc., and has research support from Pliant Therapeutics and Transcode Therapeutics. The remaining authors have no disclosures to report.

Supplemental Material

Data S1

REFERENCES

1. Fang JC, DeMarco T, Givertz MM, Borlaug BA, Lewis GD, Rame E, Gomberg-Maitland M, Murali S, Frantz RP, McGlothlin D, et al. World Health Organization pulmonary hypertension group 2: pulmonary hypertension due to left heart disease in the adult—a summary statement from the pulmonary hypertension Council of the International Society for heart and lung transplantation. *J Heart Lung Transplant*. 2012;31:913–933. doi: 10.1016/j.healun.2012.06.002
2. Vachiéry J, Adir Y, Barberà JA, Champion H, Coghlan JG, Cottin V, De Marco T, Galiè N, Ghio S, Gibbs SR, et al. Pulmonary hypertension due to left heart diseases. *J Am Coll Cardiol*. 2013;62:D100–D108. doi: 10.1016/j.jacc.2013.10.033
3. Cournand A, Bloomfield RA, Lauson HD. Double lumen catheter for intravenous and intracardiac blood sampling and pressure recording. *Proc Soc Exp Biol Med*. 1945;60:73–75. doi: 10.3181/00379727-60-15095
4. Maron BA. Revised definition of pulmonary hypertension and approach to management: a clinical primer. *J Am Heart Assoc*. 2023;12:e029024. doi: 10.1161/JAHA.122.029024
5. Voelkel NF, Quaife RA, Leinwand LA, Barst RJ, McGoon MD, Meldrum DR, Dupuis J, Long CS, Rubin LJ, Smart FW, et al. Right ventricular function and failure: report of a National Heart, Lung, and Blood Institute working group on cellular and molecular mechanisms of right heart failure. *Circulation*. 2006;114:1883–1891. doi: 10.1161/CIRCULATIONAHA.106.632208
6. Rosenkranz S, Gibbs JS, Wachter R, De Marco T, Vonk-Noordegraaf A, Vachiery JL. Left ventricular heart failure and pulmonary hypertension. *Eur Heart J*. 2016;37:942–954. doi: 10.1093/eurheartj/ehv512
7. Berthelot E, Bauer F, Eicher JC, Flecher E, Gellen B, Guihaire J, Guijarro D, Roul G, Salvat M, Tribouilloy C, et al. Pulmonary hypertension in chronic heart failure: definitions, advances, and unanswered issues. *ESC Heart Fail*. 2018;5:755–763. doi: 10.1002/ehf2.12316
8. Chen Y, Guo H, Xu D, Xu X, Wang H, Hu X, Lu Z, Kwak D, Xu Y, Gunther R, et al. Left ventricular failure produces profound lung remodeling and pulmonary hypertension in mice: heart failure causes severe lung disease. *Hypertension*. 2012;59:1170–1178. doi: 10.1161/HYPERTENSIONAHA.111.186072
9. Karuppagoundera V, Arumugama S, Babub SS, Palaniyandic SS, Watanabea K, Cookeb JP, Thandavarayanb RA. The senescence accelerated mouse prone 8 (SAMP8): a novel murine model for cardiac aging. *Ageing Res Rev*. 2017;35:291–296. doi: 10.1016/j.arr.2016.10.006
10. Shah AM, Shah SJ, Anand IS, Sweitzer NK, O'Meara E, Heitner JF, Sopko G, Li G, Assmann SF, McKinlay SM, et al. Cardiac structure and function in heart failure with preserved ejection fraction: baseline findings from the echocardiographic study of the treatment of preserved cardiac function heart failure with an aldosterone antagonist trial. *Circ Heart Fail*. 2014;7:104–115. doi: 10.1161/CIRCHEARTFAILURE.113.000887
11. Howard LS, Grapsa J, Dawson D, Bellamy M, Chambers JB, Masani ND, Nihoyannopoulos P, Simon RGJ. Echocardiographic assessment of pulmonary hypertension: standard operating procedure. *Eur Respir Rev*. 2012;21:239–248. doi: 10.1183/09059180.00003912
12. Johns CS, Kiely DG, Rajaram S, Hill C, Thomas S, Karunasaagarar K, Garg P, Hamilton N, Solanki R, Capener DA, et al. Diagnosis of pulmonary hypertension with cardiac MRI: derivation and validation of regression models. *Radiology*. 2019;290:61–68. doi: 10.1148/radiol.2018180603
13. Saunders LC, Hughes PJC, Alabed S, Capener DJ, Marshall H, Vogel-Claussen J, van Beek EJR, Kiely DG, Swift AJ, Wild JM. Integrated cardiopulmonary MRI assessment of pulmonary hypertension. *J Magn Reson Imaging*. 2022;55:633–652. doi: 10.1002/jmri.27849
14. Jansen SMA, In H, 't Veld AE, Tolen P, Jacobs W, Willemsen HM, Grotjohan HP, Waskowsky M, van der Maten J, van der Weerdt A, et al. Clinical characteristics of patients undergoing right heart catheterizations in community hospitals. *J Am Heart Assoc*. 2022;11:e025143. doi: 10.1161/JAHA.121.025143
15. Andersen S, Nielsen-Kudsk JE, Vonk Noordegraaf A, de Man FS. Right ventricular fibrosis. *Circulation*. 2019;139:269–285. doi: 10.1161/CIRCULATIONAHA.118.035326
16. Patel RB, Li E, Benefield BC, Swat SA, Polsinelli VB, Carr JC, Shah SJ, Markl M, Collins JD, Freed BH. Diffuse right ventricular fibrosis in heart failure with preserved ejection fraction and pulmonary hypertension. *ESC Heart Fail*. 2020;7:253–263. doi: 10.1002/ehf2.12565
17. Thenappan T, Prins KW, Cogswell R, Shah SJ. Pulmonary hypertension secondary to heart failure with preserved ejection fraction. *Can J Cardiol*. 2015;31:430–439. doi: 10.1016/j.cjca.2014.12.028
18. Lai YC, Wang L, Gladwin MT. Insights into the pulmonary vascular complications of heart failure with preserved ejection fraction. *J Physiol*. 2019;597:1143–1156. doi: 10.1113/JP275858
19. Désogère P, Tapias LF, Hariri LP, Rotile NJ, Rietz TA, Probst CK, Blasi F, Day H, Mino-Kenudson M, Weinreb P, et al. Type I collagen–targeted PET probe for pulmonary fibrosis detection and staging in preclinical models. *Sci Transl Med*. 2017;9:eaaf4696. doi: 10.1126/scitranslmed.aaf4696
20. Désogère P, Tapias LF, Rietz TA, Rotile N, Blasi F, Day H, Elliott J, Fuchs BC, Lanuti M, Caravan P. Optimization of a collagen-targeted PET probe for molecular imaging of pulmonary fibrosis. *J Nucl Med*. 2017;58:1991–1996. doi: 10.2967/jnumed.117.193532
21. Kapur NK, Paruchuri V, Aronovitz MJ, Qiao X, Mackey EE, Daly GH, Ughreja K, Levine J, Blanton R, Hill NS, et al. Biventricular remodeling in murine models of right ventricular pressure overload. *PLoS One*. 2013;8:e70802. doi: 10.1371/journal.pone.0070802
22. Heinzel FR, Hegemann N, Hohendanner F, Primessnig U, Grune J, Blaschke F, de Boer RA, Pieske B, Schiattarella GG, Kuebler WM. Left ventricular dysfunction in heart failure with preserved ejection fraction—molecular mechanisms and impact on right ventricular function. *Cardiovascular Diagnosis and Therapy*. 2020;10:1541–1560.
23. Frangogiannis NG. The extracellular matrix in ischemic and nonischemic heart failure. *Circ Res*. 2019;125:117–146. doi: 10.1161/CIRCRESAHA.119.311148
24. Montesi SB, Izquierdo-Garcia D, Désogère P, Abston E, Liang LL, Digumarthy S, Seethamraju R, Lanuti M, Caravan P, Catana C. Type I collagen–targeted positron emission tomography imaging in idiopathic pulmonary fibrosis: first-in-human studies. *AJRCCM*. 2019;200:258–261. doi: 10.1164/rccm.201903-0503LE
25. Izquierdo-Garcia D, Desogere P, Le Fur M, Shuvaev S, Zhou IY, Ramsay I, Lanuti M, Catalano OA, Catana C, Caravan P, et al. Biodistribution, dosimetry, and pharmacokinetics of (68)Ga-CBP8: a type I collagen-targeted PET probe. *J Nucl Med*. 2023;64:775–781. doi: 10.2967/jnumed.122.264530
26. Chen HH, Waghorn PA, Wei L, Tapias LF, Schuhle DT, Rotile NJ, Jones CM, Looby RJ, Zhao G, Elliott JM, et al. Molecular imaging of oxidized collagen quantifies pulmonary and hepatic fibrogenesis. *JCI Insight*. 2017;2:e91506. doi: 10.1172/jci.insight.91506
27. Waghorn PA, Jones CM, Rotile NJ, Koerner SK, Ferreira DS, Chen HH, Probst CK, Tager AM, Caravan P. Molecular magnetic resonance imaging of lung fibrogenesis with an oxyamine-based probe. *Angew Chem Int Ed Engl*. 2017;56:9825–9828. doi: 10.1002/anie.201704773
28. Akam EA, Abston E, Rotile NJ, Slattery HR, Zhou IY, Lanuti M, Caravan P. Improving the reactivity of hydrazine-bearing MRI probes for in vivo imaging of lung fibrogenesis. *Chem Sci*. 2020;11:224–231. doi: 10.1039/c9sc04821a
29. Ning Y, Zhou IY, Roberts JD. Molecular MRI quantification of extracellular aldehyde pairs for early detection of liver fibrogenesis and response to treatment. *Sci Transl Med*. 2022;14:eabq6297. doi: 10.1126/scitranslmed.abq6297

30. Ning Y, Zhou IY, Rotile NJ, Pantazopoulos P, Wang H, Barrett SC, Sojoodi M, Tanabe KK, Caravan P. Dual hydrazine-equipped turn-on manganese-based probes for magnetic resonance imaging of liver fibrogenesis. *J Am Chem Soc*. 2022;144:16553–16558. doi: 10.1021/jacs.2c06231
31. Chen Y, Waghorn PA, Rosales IA, Arora G, Erstad DJ, Rotile NJ, Jones CM, Ferreira DS, Wei L, Martinez RVP, et al. Molecular MR imaging of renal fibrogenesis in mice. *J Am Soc Nephrol*. 2023;34:1159–1165. doi: 10.1681/ASN.0000000000000148
32. Zhou IY, Jordan VC, Rotile NJ, Akam E, Krishnan S, Arora G, Krishnan H, Slattery H, Warner N, Mercaldo N, et al. Advanced MRI of liver fibrosis and treatment response in a rat model of nonalcoholic steatohepatitis. *Radiology*. 2020;296:67–75. doi: 10.1148/radiol.2020192118
33. Waghorn PR, Ferreira DS, Erstad DJ, Rotile NJ, Masia R, Jones CM, Tu C, Sojoodi M, Chen YI, Schlerman F, et al. Quantitative, noninvasive MRI characterization of disease progression in a mouse model of non-alcoholic steatohepatitis. *Sci Rep*. 2021;11:6105. doi: 10.1038/s41598-021-85679-4
34. Ma H, Zhou I, Chen YI, Rotile N, Ay I, Akam EA, Wang H, Knipe RS, Hariri LP, Zhang C, et al. Tailored chemical reactivity probes for systemic imaging of aldehydes in fibroproliferative diseases. *J Am Chem Soc*. 2023;145:20825–20836. doi: 10.1021/jacs.3c04964
35. Richards DA, Aronovitz MJ, Calamaras TD, Tam K, Martin GL, Liu P, Bowditch HK, Zhang P, Huggins GS, Blanton RM. Distinct phenotypes induced by three degrees of transverse aortic constriction in mice. *Sci Rep*. 2019;9:5844. doi: 10.1038/s41598-019-42209-7
36. *Guide for the Care and Use of Laboratory Animals*, *8th edition*. Washington (DC): National Academies Press (US); 2011.
37. Mueller D, Breeman WAP, Klette I, Gottschaldt M, Odparlik A, Baehre M, Tworowska I, Schultz MK. Radiolabeling of DOTA-like conjugated peptides with generator-produced 68Ga and using NaCl-based cationic elution method. *Nat Protoc*. 2016;11:1057–1066. doi: 10.1038/nprot.2016.060
38. Loening AM, Gambhir SS. AMIDE: a free software tool for multimodality medical image analysis. *Mol Imaging*. 2003;2:131–137. doi: 10.1162/15353500200303133
39. Schipke J, Brandenberger C, Rajces A, Manninger M, Alogna A, Post H, Mühlfeld C. Assessment of cardiac fibrosis: a morphometric method comparison for collagen quantification. *J Appl Physiol*. 2017;122:1019–1030. doi: 10.1152/japplphysiol.00987.2016
40. Li X, Fang Z, Guan T, Lin J, Sun C, Huang S, Mao R, Lu B, Cao Q, Feng S, et al. A novel collagen area fraction index to quantitatively assess bowel fibrosis in patients with Crohn's disease. *BMC Gastroenterol*. 2019;19:180. doi: 10.1186/s12876-019-1100-3
41. Bhedi CD, Nasirova S, Toksoz D, Warburton RR, Morine KJ, Kapur NK, Galper JB, Preston IR, Hill NS, Fanburg BL, et al. Glycolysis regulated transglutaminase 2 activation in cardiopulmonary fibrogenic remodeling. *FASEB J*. 2020;34:930–944. doi: 10.1096/fj.201902155R
42. Schaller MA, Sharma Y, Dupee Z, Nguyen D, Urueña J, Smolchek R, Loeb JC, Machuca TN, Lednicky JA, Odde DJ, et al. Ex vivo SARS-CoV-2 infection of human lung reveals heterogeneous host defense and therapeutic responses. *JCI Insight*. 2021;6:e148003. doi: 10.1172/jci.insight.148003
43. Hutson PR, Crawford ME, Sorkness RL. Liquid chromatographic determination of hydroxyproline in tissue samples. *J Chromatogr B*. 2003;791:427–430. doi: 10.1016/S1570-0232(03)00248-4
44. Waghorn PA, Oliveira BL, Jones CM, Tager AM, Caravan P. High sensitivity HPLC method for determination of the allysine concentration in tissue by use of a naphthol derivative. *J Chromatogr B Analyt Technol Biomed Life Sci*. 2017;1064:7–13. doi: 10.1016/j.jchromb.2017.08.032
45. Borlaug BA. Evaluation and management of heart failure with preserved ejection fraction. *Nat Rev Cardiol*. 2020;17:559–573. doi: 10.1038/s41569-020-0363-2
46. Triposkiadis F, Xanthopoulos A, Butler J. Cardiovascular aging and heart failure: JACC review topic of the week. *J Am Coll Cardiol*. 2019;74:804–813. doi: 10.1016/j.jacc.2019.06.053
47. Paulus WJ, Zile MR. From systemic inflammation to myocardial fibrosis: the heart failure with preserved ejection fraction paradigm revisited. *Circ Res*. 2021;128:1451–1467. doi: 10.1161/CIRCRESAHA.121.318159
48. Alex L, Russo I, Holoborodko V, Frangogiannis NG. Characterization of a mouse model of obesity-related fibrotic cardiomyopathy that recapitulates features of human heart failure with preserved ejection fraction. *Am J Physiol Heart Circ Physiol*. 2018;315:H934–H949. doi: 10.1152/ajpheart.00238.2018
49. Penumatsa KC, Falcao-Pires I, Leite S, Leite-Moreira A, Bhedi CD, Nasirova S, Ma J, Sutliff RL, Fanburg BL. Increased transglutaminase 2 expression and activity in rodent models of obesity/metabolic syndrome and aging. *Front Physiol*. 2020;11:560019. doi: 10.3389/fphys.2020.560019
50. Caravan P, Yang Y, Zachariah R, Schmitt A, Mino-Kenudson M, Chen HH, Sosnovik DE, Dai G, Fuchs BC, Lanuti M. Molecular magnetic resonance imaging of pulmonary fibrosis in mice. *Am J Respir Cell Mol Biol*. 2013;49:1120–1126. doi: 10.1165/rcmb.2013-0039OC
51. Caravan P, Das B, Dumas S, Epstein FH, Helm PA, Jacques V, Koerner S, Kolodziej A, Shen L, Sun W, et al. Collagen-targeted MRI contrast agent for molecular imaging of fibrosis. *Angew Chem Int Ed Engl*. 2007;46:8171–8173. doi: 10.1002/anie.200700700
52. Helm PA, Caravan P, French BA, Jacques V, Shen L, Xu Y, Beyers RJ, Roy RJ, Kramer CM, Epstein FH. Postinfarction myocardial scarring in mice: molecular MR imaging with use of a collagentargeting contrast agent. *Radiology*. 2008;247:788–796. doi: 10.1148/radiol.2473070975
53. Farrar CT, DePeralta DK, Day H, Rietz TA, Wei L, Lauwers GY, Keil B, Subramaniam A, Sinskey AJ, Tanabe KK, et al. 3D molecular MR imaging of liver fibrosis and response to rapamycin therapy in a bile duct ligation rat model. *J Hepatol*. 2015;63:689–696. doi: 10.1016/j.jhep.2015.04.029
54. Polasek M, Fuchs BC, Uppal R, Schühle DT, Alford JK, Loving GS, Yamada S, Wei L, Lauwers GY, Guimaraes AR, et al. Molecular MR imaging of liver fibrosis: a feasibility study using rat and mouse models. *J Hepatol*. 2012;57:549–555. doi: 10.1016/j.jhep.2012.04.035
55. Fuchs BC, Wang H, Yang Y, Wei L, Polasek M, Schühle DT, Lauwers GY, Parkar A, Sinskey AJ, Tanabe KK, et al. Molecular MRI of collagen to diagnose and stage liver fibrosis. *J Hepatol*. 2013;59:992–998. doi: 10.1016/j.jhep.2013.06.026
56. Jandl K, Radic N, Zeder K, Kovacs G, Kwapiszewska G. Pulmonary vascular fibrosis in pulmonary hypertension—the role of the extracellular matrix as a therapeutic target. *Pharmacol Ther*. 2023;247:108438. doi: 10.1016/j.pharmthera.2023.108438
57. Jandl K, Marsh LM, Mutgan AC, Crnkovic S, Valzano F, Zabini D, Hoffmann J, Foris V, Gschwandtner E, Klepetko W, et al. Impairment of the NKT–STAT1–CXCL9 Axis contributes to vessel fibrosis in pulmonary hypertension caused by lung fibrosis. *Am J Respir Crit Care Med*. 2022;206:981–998. doi: 10.1164/rccm.202201-0142OC
58. Milara J, Roger I, Montero P, Artigues E, Escrivá J, Cortijo J. IL-11 system participates in pulmonary artery remodeling and hypertension in pulmonary fibrosis. *Respir Res*. 2022;23:313. doi: 10.1186/s12931-022-02241-0
59. Kim RJ, Fieno DS, Parrish TB, Harris K, Chen EL, Simonetti O, Bundy J, Finn JP, Klocke FJ. Relationship of MRI delayed contrast enhancement to irreversible injury, infarct age, and contractile function. *Circulation*. 1999;100:1992–2002. doi: 10.1161/01.cir.100.19.1992
60. Kim RJ, Wu E, Rafael A, Chen EL, Parker MA, Simonetti O, Klocke FJ, Bonow RO, Judd RM. The use of contrast-enhanced magnetic resonance imaging to identify reversible myocardial dysfunction. *N Engl J Med*. 2000;343:1445–1453. doi: 10.1056/NEJM200011163432003
61. Simonetti OP, Kim RJ, Fieno DS, Hillenbrand HB, Wu E, Bundy JM, Finn JP, Judd RM. An improved MR imaging technique for the visualization of myocardial infarction. *Radiology*. 2001;218:215–223. doi: 10.1148/radiology.218.1.r01ja50215
62. Haaf P, Garg P, Messroghli DR, Broadbent DA, Greenwood JP, Plein S. Cardiac T1 mapping and extracellular volume (ECV) in clinical practice: a comprehensive review. *J Cardiovasc Magn Reson*. 2016;18:89. doi: 10.1186/s12968-016-0308-4
63. Moon JC, Messroghli DR, Kellman P, Piechnik SK, Robson MD, Ugander M, Gatehouse PD, Arai AE, Friedrich MG, Neubauer S, et al. Myocardial T1 mapping and extracellular volume quantification: a Society for Cardiovascular Magnetic Resonance (SCMR) and CMR working Group of the European Society of cardiology consensus statement. *J Cardiovasc Magn Reson*. 2013;15:92. doi: 10.1186/1532-429X-15-92
64. Skavdahl M, Steenbergen C, Clark J, Myers P, Demianenko T, Mao L, Rockman HA, Korach KS, Murphy E. Estrogen receptor-beta mediates male-female differences in the development of pressure overload hypertrophy. *Am J Physiol Heart Circ Physiol*. 2005;288:H469–H476. doi: 10.1152/ajpheart.00723.2004
65. Fliegner D, Schubert C, Penkalla A, Witt H, Kararigas G, Dworatzek E, Staub E, Martus P, Noppinger PR, Kintscher U, et al. Female sex and estrogen receptor-beta attenuate cardiac remodeling and apoptosis in pressure overload. *Am J Physiol Regul Integr Comp Physiol*. 2010;298:R1597–R1606. doi: 10.1152/ajpregu.00825.2009